Journal of Materials Chemistry A

PAPER

View Article Online
View Journal | View Issue



Cite this: J. Mater. Chem. A, 2016, 4, 8866

# 3D $Fe_3O_4$@Au@Ag nanoflowers assembled magnetoplasmonic chains for *in situ* SERS monitoring of plasmon-assisted catalytic reactions†

Qianqian Ding,[ab] Hongjian Zhou,*[a] Haimin Zhang,[a] Yunxia Zhang,[a] Guozhong Wang[a] and Huijun Zhao*[ac]

Received 17th March 2016
Accepted 9th May 2016

DOI: 10.1039/c6ta02264b

www.rsc.org/MaterialsA

One-dimensional (1D) assembled magnetoplasmonic nanochains (MPNCs) were fabricated using $Fe_3O_4$@Au core–shell nanoparticles (NPs) *via* a magnetic field induced assembly. With the help of a silver growth solution, the 3D $Fe_3O_4$@Au@Ag nanoflowers assembled magnetoplasmonic chains ($Fe_3O_4$@Au@Ag NAMPCs) were prepared *via* an *in situ* reduction method. A heterogeneous epitaxial growth mechanism was proposed to explain the growth process of the $Fe_3O_4$@Au@Ag NAMPCs. The $Fe_3O_4$@Au@Ag NAMPCs possessed large numbers of hot spots within the highly ordered structure and were used as a SERS substrate to enhance the sensitivity, uniformity and reproducibility of Raman signals. Subsequently, the $Fe_3O_4$@Au@Ag NAMPCs, integrating a heterogeneous catalysis and *in situ* SERS detection, was assessed to monitor the catalytic reduction of 4-nitrothiophenol (4-NTP) to *p,p*′-dimercaptoazobenzene (DMAB).

## 1. Introduction

Owning to its non-destructive nature, surface-enhanced Raman spectroscopy (SERS) has been widely recognized as an effective monitoring tool for studying reaction processes *in situ*.[1–5] In comparison to other sensing techniques, an ability to carry out near real-time monitoring of a reaction process *in situ* without destructing the innate reaction process is a distinctive advantage of the SERS technique.[6,7] As such, the nature of the transient reaction intermediates and mechanistic pathways involved in heterogeneously catalyzed chemical reactions can be obtained using the SERS technique.[8] The SERS technique is capable of providing useful information for mechanistic studies and reaction system optimization. Thus, characterization of the binding and/or reaction of adsorbates at the surfaces of metals using the SERS technique is of great importance for understanding and improving catalytic reactions.[9] Nevertheless, insufficient sensitivity and reproducibility resulting from the poor SERS substrate quality has greatly limited the applicability of SERS as an *in situ* monitoring technique for a wide variety of reaction systems. An extensive research effort has therefore been diverted to develop a SERS substrate with enhanced sensing signal.[10–13] In this regard, functional metallic and plasmonic arrays-based SERS substrates have been demonstrated to be effective for SERS performance enhancement. Recently, one-dimensional (1D) nanostructured metallic SERS substrates have drawn a lot of attention because of their absorption shift associated with longitudinal resonances extended into the infrared region and the benefits offered by the coupling effect of the 1D plasmonic metallic array to enhance the sensitivity of the SERS signals.[14,15] Interestingly, SERS substrates made of multi-metallic components can serve dual functions as a SERS signal generator and catalyst, which is advantageous for *in situ* studies of a catalytic reaction process.

It has been confirmed that assembling metallic nanoparticles (NPs) into highly ordered structures on suitable surfaces can be used to significantly enhance the sensitivity and reproducibility of SERS signals.[16,17] Lee and co-workers reported that a facile method based on capillarity-assisted assembly was used to fabricate high-performance SERS substrates employing clean Au NPs.[18,19] Cai and co-workers have fabricated highly sensitive and reproducible SERS substrates using the periodic arrays method *via* a sputtering deposition method based on a colloidal monolayer template.[20,21] In the assembly process, a high temperature calcination or organic solvent self-assembly

[a]Key Laboratory of Materials Physics, Centre for Environmental and Energy Nanomaterials, Anhui Key Laboratory of Nanomaterials and Nanotechnology, Institute of Solid State Physics, Chinese Academy of Sciences, Hefei 230031, P. R. China. E-mail: hjzhou@issp.ac.cn

[b]Department of Materials Science and Engineering, University of Science and Technology of China, Hefei 230026, P. R. China

[c]Centre for Clean Environment and Energy, Gold Coast Campus, Griffith University, QLD 4222, Australia. E-mail: h.zhao@griffith.edu.au

† Electronic supplementary information (ESI) available: Experimental details, SEM and TEM images of $Fe_3O_4$@Au@Ag NAMPCs and the $Fe_3O_4$@Au@Ag NAMPCs as SERS substrate to monitor of catalytic reaction of 4-NTP to DMAB. See DOI: 10.1039/c6ta02264b

process was carried out, which would reduce the sensitivity of SERS. However, the speedy and moderate conditions for the *in situ* fabrication of highly sensitive and reproducible SERS substrates are required in their practical applications.

We have recently reported a series of investigations on the new properties and assembly behavior of magnetoplasmonic nanomaterials.[22] We demonstrated that magneto-plasmonic $Fe_3O_4$@Au core–shell NPs can be assembled in a highly ordered form of 1D magnetoplasmonic nanochains (MPNCs) under the influence of an applied external static magnetic field.[23,24] However, when used as a SERS substrate, the resultant MPNCs exhibited unsatisfactory SERS sensitivity, poor uniform signal intensity distribution and low SERS performance reproducibility between the substrates obtained from different batches, which was mainly due to the uneven distribution and large inter-spaces of the assembled NPs.[25,26] The hierarchical nanostructure arrays possess a high surface area with rich surface chemistry, which is beneficial to capturing the analyte and an increase in the number of hot spots in a large volume will enhance the SERS-activity. Therefore, 3D $Fe_3O_4$@Au@Ag nanoflowers assembled magnetoplasmonic chains ($Fe_3O_4$@Au@Ag NAMPCs) with high-density 3D "hot spots" are expected to have highly sensitive and reproducible SERS signals.

Plasmon-assisted heterogeneous catalysis has been recently investigated using SERS in which the localized surface plasmon resonance (LSPR) in the metal nanostructures of the SERS substrate facilitates the charge-transfer photochemistry *via* enhancement of the local electromagnetic field intensity. For example, Tang *et al.*[27] have used a silver microflower single structure to monitor the plasmon-assisted reduction of 4-nitrothiophenol (4-NTP) to *p*,*p*′-dimercaptoazobenzene (DMAB) *in situ*. Kang *et al.*[28–30] have used single particle surface enhanced Raman spectroscopy to monitor power-dependent plasmon-driven chemical reactions. Zhang *et al.*[31,32] found that the electric field gradient leads to a strong enhancement of the infrared (IR)-active modes of DMAB. Tian *et al.*[33,34] confirmed the chemical transformation of 4-NTP to DMAB through experiments and theoretical calculations. However, the low reproducibility of these complicated syntheses is a serious obstacle to the understanding of the surface catalysis coupling reaction process. Even though some important results have been achieved, previous studies have ignored the significant relationship between the reaction speed, the laser exposure and laser power. In the context of understanding plasmon-enhanced coupling, the oxidative dimerisation of 4-NTP to DMAB on $Fe_3O_4$@Au@Ag NAMPCs was selected as a model reaction for the demonstration of *in situ* SERS monitoring with uniform signal intensity distribution and high reproducibility.

In this study, the $Fe_3O_4$@Au@Ag NAMPCs were successfully fabricated as a SERS-active substrate and was constructed from 3D nanoflower shaped silver nanoplates coated on MPNCs *via* a magnetic field induced assembly. The hierarchical nanostructure arrays possess highly ordered structures, Au/Ag interface, vast surface area and nanoscale roughness, which are beneficial for enhancing the sensitivity, uniformity and reproducibility of the Raman signal. Moreover, the $Fe_3O_4$@Au@Ag NAMPCs, integrating a heterogeneous catalysis and *in situ* SERS detection, were evaluated as a dual-function SERS substrate for *in situ* SERS monitoring of a catalytic reaction process in kinetic studies by varying the duration of laser exposure and laser power (Scheme 1).

## 2. Experimental

### 2.1 Materials

$HAuCl_4 \cdot 3H_2O$ (99.9%), $Na_3C_6H_5O_7$, $FeCl_3 \cdot 6H_2O$, $AgNO_3$, 4-nitrothiophenol, $C_6H_6O_2$, rhodamine (R6G) and crystal violet (CV) were obtained from Sigma Aldrich Ltd. Ammonia solution (28% w/v) was procured from Shanghai Chemical Reagent Company (Shanghai, China). Silicon wafer was procured from Kejing Materials Technology Company Ltd (Hefei, China). Deionized water (>18.2 mΩ $cm^{-1}$) was purified using a Millipore Milli-Q gradient system and was used throughout the experiments. All chemicals were of analytical grade and used as received.

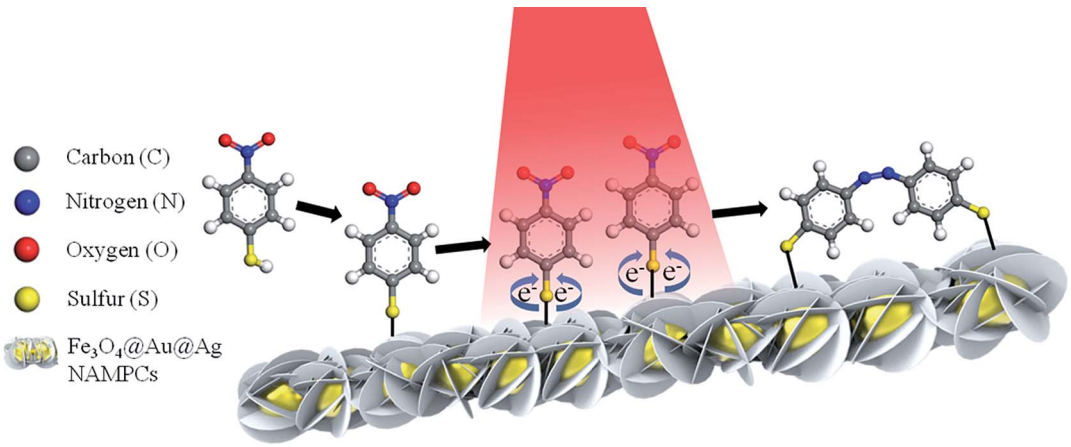


Scheme 1 Schematic of SERS monitoring in the catalytic reaction of 4-nitrobenzenethiol dimerization to form *p*,*p*′-dimercaptoazobenzene on the $Fe_3O_4$@Au@Ag NAMPCs.

### 2.2 Fabrication of the $Fe_3O_4$@Au@Ag NAMPCs

The 1D MPNCs were assembled on a silicon wafer *via* an external magnetic force according to our previous reports.[23,35] The silver nanoplates were grown on the MPNCs to form $Fe_3O_4$@Au@Ag NAMPCs using a silver growth solution. First, a citrate buffer solution (pH = 3.6) of hydroquinone was prepared by dissolving 0.10 M citric acid, 0.10 M trisodium citrate dehydrate and 0.10 M hydroquinone in deionized water. The silver growth solution was made by mixing 1.70 mL of the citrate buffer solution of hydroquinone with 0.30 mL of a silver ion solution (0.10 M $AgNO_3$). The as-prepared MPNCs were incubated with the silver growth solution for the different times under dark conditions. The sample was then washed with deionized water and dried under nitrogen gas. The irregular $Fe_3O_4$@Au@Ag NPs were prepared as a reference on the $Fe_3O_4$@Au NPs *via* the same method but without an external magnetic field. All the samples were prepared on a silicon wafer and can be used as the SERS substrate after being washed with deionized water.

### 2.3 Surface-enhanced Raman spectroscopy (SERS) measurements

The $Fe_3O_4$@Au MPNCs, irregular $Fe_3O_4$@Au@Ag NPs and $Fe_3O_4$@Au@Ag NAMPCs as SERS substrates were functionalized with the analyte solution (R6G or CV) at concentrations in the range of $10^{-7}$ to $10^{-11}$ M for 30 min by chemisorption. Then, the SERS substrate was rinsed with deionized water to remove the unabsorbed molecules. Finally, the substrates were dried using a flow of nitrogen prior to the SERS measurement. The Raman spectra were obtained using a confocal microscopy Raman spectrometer coupled with microscope using a 100× objective. The laser power at the sample position was 0.5 mW, the laser beam was focused on the sample in a size of about 1.5 μm and the typical accumulation time used for the study was 2 s.

### 2.4 *In situ* SERS monitoring of the catalytic reaction

The reduction of 4-NTP to DMAB by the $Fe_3O_4$@Au@Ag NAMPCs was carried out to examine the catalytic activity under different excitation power. The $Fe_3O_4$@Au@Ag NAMPCs substrate was immersed in the 4-NTP ($10^{-4}$ M) solution for 1 h. Then, the $Fe_3O_4$@Au@Ag NAMPCs were rinsed repeatedly with deionized water to remove the residual 4-NTP. After being dried at room temperature, lasers with different excitation powers were used as changeable conditions to get the different reaction rates.

### 2.5 Characterization

The morphologies of the MPNCs and $Fe_3O_4$@Au@Ag NAMPCs were characterized by FE-SEM (S-4700, Hitachi, Japan). Transmission electron microscopy (TEM) images were recorded using a high resolution TEM (JEOL, JEM 2010, Japan), equipped with X-ray energy dispersive spectroscopy (EDS) capabilities, operated at an acceleration voltage of 200 kV. Raman spectra were carried out on a confocal microscope Raman system (LabRAM HR800, Horiba Jobin Yvon, Japan) using an Ar ion laser operating at 632.8 nm. The laser power was selected according to the experimental conditions. The magnetic properties of the nanomaterials were measured using a superconducting quantum interference device (SQUID) magnetometer (MPMS XL-7, Quantum Design, USA).

## 3. Results and discussion

### 3.1 Fabrication of the $Fe_3O_4$@Au@Ag NAMPCs on a silicon wafer substrate

The $Fe_3O_4$@Au NPs were used as building blocks to fabricate 1D MPNCs *via* a magnetic field induced assembly. The SEM images of the MPNCs are shown in Fig. 1A and B. On the microscale, the $Fe_3O_4$@Au NPs are aligned along the magnetic flux of the external magnetic field, owing to their superparamagnetism. The MPNCs exhibited lengths of over 100 μm and widths of about 500 nm (Fig. 1A). On the nanoscale, the randomly aggregated $Fe_3O_4$@Au NPs are clearly observed as building blocks to the formed MPNCs (Fig. 1B). The assembly mechanism of the MPNCs was described in our previous report.[35] Fig. S1 (see ESI†) shows the UV-Vis absorption, hysteresis loop and TEM images of the $Fe_3O_4$@Au NPs. The TEM image showed that the average size of the $Fe_3O_4$@Au NPs was about 20 nm and the UV-Vis absorption peak of the $Fe_3O_4$@Au NPs was around 541 nm, owing to the Au shell completely coating the surface of the $Fe_3O_4$ NPs. The saturation magnetization value of the $Fe_3O_4$@Au NPs was 16.15 emu $g^{-1}$. The $Fe_3O_4$@Au NPs were also characterized by HRTEM (Fig. S2F, see ESI†), which showed the presence of Au (fringe spacing = 0.236 nm) out of the $Fe_3O_4$ NPs.

To produce high performance SERS substrate using the 1D assembled nanostructure, the as-prepared MPNCs were treated with a silver growth solution. Silver nanoplates were grown onto the gold surface of the MPNCs. The gold surface acts as a nucleation site and catalyst and significantly accelerates the silver growth process. The morphology of the $Fe_3O_4$@Au@Ag NAMPCs is shown in Fig. 1C and D. It can be observed that

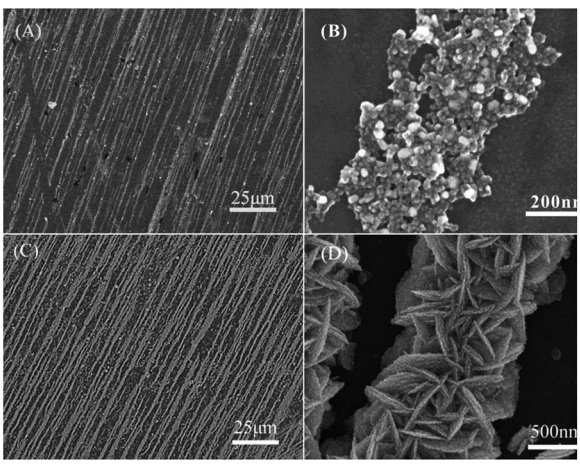


Fig. 1 The SEM image of (A) the MPNCs and (B) the magnified image of the MPNCs. The SEM image of (C) the $Fe_3O_4$@Au@Ag NAMPCs and (D) the magnified image of the $Fe_3O_4$@Au@Ag NAMPCs.

 

consecutive silver nanoplates are grown on the surface of the MPNCs. The diameter of the $Fe_3O_4$@Au@Ag NAMPCs was about 1.5 μm and the thickness of one nanoplate was 15 nm. Interpenetrating silver nanoplates stand on the surface of the MPNCs with sharp edges, resulting in an overall nanoplate shape with an enlarged surface. It can be noted that the $Fe_3O_4$@Au@Ag NAMPCs provided extra surface areas at the Au/Ag interface, which significantly increases its SERS-active properties. Multilayer Au/Ag interface arrays on the $Fe_3O_4$@Au@Ag NAMPCs can induce localized surface plasmon resonance (LSPR) effects owing to the interface gap effect and the availability of multiple edges and small curvature.[36] It has been indicated that the repeated layer of the Au/Ag nanostructure is most likely responsible for the formation of a large EM field in the vicinity of the interface.[37]

Understanding the growth mechanism is crucial for optimizing the synthetic conditions and designing other unconventional structures by adopting this approach. We also investigated the growth process of the $Fe_3O_4$@Au@Ag NAMPCs with different growth times using SEM. The time evolution of $Fe_3O_4$@Au@Ag NAMPCs is illustrated in Fig. 2. At the primary stage, the Ag nanoplates were formed on the MPNCs at 5 min growth time (Fig. 2A). The Ag nanoplates both perpendicular to and lying on the substrate could be observed, and the sizes in each direction were nearly same. However, the distribution density of the Ag nanoplates was relatively low and a certain amount of the $Fe_3O_4$@Au NPs were still uncoated. With the growth time prolonged to 10 min (Fig. 2B), both the size and the distribution density of the Ag nanoplates were increased. Moreover, the Ag nanoplates show a preferential growth direction that was perpendicular to the $Fe_3O_4$@Au NPs. By comparing Fig. 2A and B, the Ag nanoplates showed an outward growth. Growing to an extent (Fig. 2C), the adjoining nanoplates connect with each other and then the contact site becomes a nucleation site for further growth. When the growth time was as long as 20 min (Fig. 2D), the $Fe_3O_4$@Au NPs were all coated with Ag nanoplates. The crossed Ag nanoplates became dense, but still remain a layered structure.

The morphology evolution of the 3D Ag nanoflower was also checked using TEM over time during the reaction (Fig. 3). The 3D Ag nanoflower has a hierarchical structure and every nanopetal was deposited with the small nanoplates. Initially the nucleation growth of the Ag nanoplates was generated on the $Fe_3O_4$@Au NPs (Fig. 3A). The Ag nanoplates were only grown out from the $Fe_3O_4$@Au NPs and the lattice fringes with a lattice spacing of about 0.25 nm corresponds to the (111) plane of the Ag crystal and the nanoplates were the single crystal structure.[38] After 5 min of growth, the Ag nanoplates developed into the petals structure and coated the $Fe_3O_4$@Au NPs (Fig. 3B). With continuous growth, the $Fe_3O_4$@Au NPs could not act as the nucleation site again, due to the whole surface being covered by the Ag nanoplates. When the reaction time reached 20 min, the small Ag nanoplates were assembled into a continuous $Fe_3O_4$@Au@Ag NAMPCs structural unit. Fig. 3C shows the TEM images of the $Fe_3O_4$@Au@Ag NAMPCs, which show that the $Fe_3O_4$@Au NPs were in an ordered arrangement and the $Fe_3O_4$@Au NPs were surrounded by the Ag nanoplates. Fig. 3D are the magnified TEM images, which show that the nanoplates in the $Fe_3O_4$@Au@Ag NAMPCs have a lamellar structure and that the boundaries between the nanoplates are clearly observed. This structure suggested a self-assembly procedure by the oriented growth and that one petal of the $Fe_3O_4$@Au@Ag NAMPCs was also the nanoplate structure. The small Ag nanoplates showed orientated growth on the $Fe_3O_4$@Au NPs in the growth solution. Upon increasing the reaction time, the small Ag nanoplates become nucleation sites for further growth. Therefore, the heterogeneous epitaxial growth of the $Fe_3O_4$@Au@Ag NAMPCs was proposed due to the $Fe_3O_4$@Au NPs of the 1D MPNCs providing the nucleation sites for growth of small Ag nanoplates and the small Ag nanoplates subsequently produced act as building blocks to assemble the Ag nanopetals. Finally, the contact sites of the Ag nanoplates transform into the nucleation sites for the assembly of 3D nanoflowers.

Moreover, the typical XRD patterns of the $Fe_3O_4$@Au NPs and $Fe_3O_4$@Au@Ag NAMPCs were measured, as shown in Fig. S1D (see ESI†). The XRD peaks of the $Fe_3O_4$@Au NPs fitted well to the Au bulk phases (JCPDS no. 04-0784) and $Fe_3O_4$ bulk

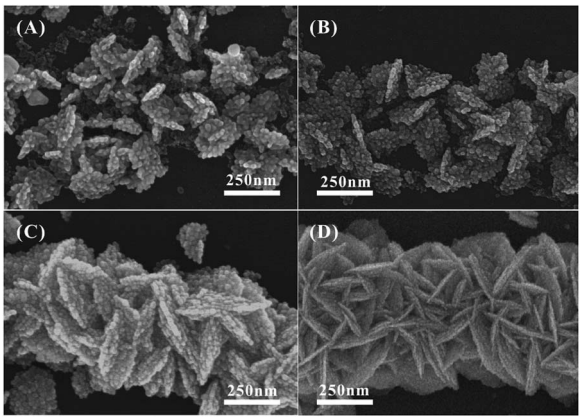


Fig. 2 SEM images of the $Fe_3O_4$@Au@Ag NAMPCs with different growth times: (A) 5 min, (B) 10 min, (C) 15 min and (D) 20 min. All other conditions remained unchanged.

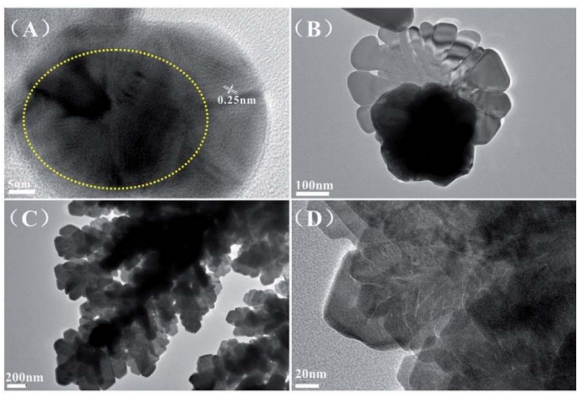


Fig. 3 TEM images of the $Fe_3O_4$@Au@Ag NAMPCs obtained with various growing times: (A) 1 min, (B) 5 min and (C) 20 min. (D) The magnified TEM images of (C).

phases (JCPDS card no. 75-1609). No additional peaks appeared after coating the Ag nanoplates because the same XRD peak positions were observed for the Au bulk phases and the Ag phases (JCPDS 87-0720). The EDAX spectrum of the $Fe_3O_4$@Au@Ag NAMPCs (Fig. S1G, see ESI†) confirmed the presence of Ag, Au, Fe and O elements.

### 3.2 SERS performance

In this study, we selected $10^{-7}$ M R6G as the probe molecule used to investigate the SERS performance of the MPNCs, irregular $Fe_3O_4$@Au@Ag NPs and the 3D $Fe_3O_4$@Au@Ag NAMPCs. The SEM images of the SERS substrates are shown in Fig. S2 (see ESI†). The 1D MPNCs exhibited a low density of nanoparticles and the big gap between the nanoparticles is shown in Fig. S2A.† Thus, the 1D MPNCs as a SERS substrate have low SERS activity. The $Fe_3O_4$@Au@Ag NAMPCs were synthesized on the 1D MPNCs using the silver growth solution; the silver nanoplates were grown onto the gold surface of the MPNCs and assembled to three-dimensional (3D) nanoflowers. The irregular $Fe_3O_4$@Au@Ag NPs were prepared on the $Fe_3O_4$@Au NPs *via* the same method but without an external magnetic field. 3D SERS-active substrates with considerable extension from 2D to 3D brings a larger overall surface area, enabling more target molecules to be adsorbed and increases the number and utility of SERS hotspots in all three dimensions.[39] Therefore, the $Fe_3O_4$@Au@Ag NAMPCs with 3D nanoflower structure could produce hotspots between the adjacent nanoplates in 3D space. Because of the 3D hotspot matrix and the high density of the nanoparticles, the $Fe_3O_4$@Au@Ag NAMPCs exhibited a higher SERS enhancement than the MPNCs and irregular $Fe_3O_4$@Au@Ag nanoparticles, as shown in Fig. 4. The high surface area of the $Fe_3O_4$@Au@Ag NAMPCs for probe adsorption was also beneficial for trapping and capturing the probe molecules to improve the SERS performance.

The SERS signals originates from the localized surface plasmons, which is dependent on the size, shape, composition, and dielectric character of the nanoparticles.[40–43] The well-ordered nanoparticles, assembled under magnetic force, exhibit a remarkable SPR property, giving a strong local electromagnetic field, which can bring forth contributions to the vibrational modes with Raman activity. The optical response of the $Fe_3O_4$@Au@Ag NAMPCs is dominated by the plasmon mode associated with the core of $Fe_3O_4$@Au and the shell of Ag nanoplates and can be rationalized in terms of plasmon hybridization. This hybridization results in a complex, multi-peaked optical spectrum, which induced a red-shift in the collective plasmon modes when compared with the $Fe_3O_4$@Au NPs. From the UV-Vis absorption spectra of the $Fe_3O_4$@Au@Ag NAMPCs (Fig. S1C, see ESI†), we can clearly observe that the $Fe_3O_4$@Au@Ag NAMPCs display two distinct plasmonic features: two shoulders located at *ca.* 540 and 650 nm. Near IR light (632.8 nm) could be largely absorbed and trapped by the $Fe_3O_4$@Au@Ag NAMPCs due to their strong absorbance in the near IR region. Therefore, the $Fe_3O_4$@Au@Ag NAMPCs have high SERS activity using the 632.8 nm laser as an excitation source.

The limit of detection is an important criterion for the SERS sensitivity of the $Fe_3O_4$@Au@Ag NAMPCs. Thus, detection of R6G using the SERS spectra with the $Fe_3O_4$@Au@Ag NAMPCs substrates was carried out. Fig. S3A (see ESI†) shows the results of the SERS spectra with different concentrations of R6G from $10^{-7}$ to $10^{-11}$ M on the substrate. Fig. S3B (see ESI†) illustrates the corresponding plot of $I_{SERS}$ *versus* $-\log$[R6G], in which $I_{SERS}$ is the SERS intensity of the recorded R6G bands at 1370 $cm^{-1}$. It demonstrates that a good linear response was achieved within the range of $10^{-7}$ M to $10^{-11}$ M R6G and concentrations as low as $10^{-11}$ M can be accurately detected using the described SERS assay.

Therefore, the assembled $Fe_3O_4$@Au@Ag NAMPCs with the strongest Raman enhancement were chosen to carry out the following experiments. The SERS enhancement factor (EF) is one of the major parameter for characterizing the SERS effect. The EF strongly depends on the exact SERS conditions: substrate, analyte, excitation wavelength and so on. Notably, the characterization of EF was carried out under identical experimental conditions (laser wavelength, laser power, microscope objective or lenses, spectrometer) and the same preparation conditions. We selected one of the important and representative definitions to calculate the EF. The definition of the SERS EF is shown in the following equation:[44]

$$\mathrm{EF} = \frac{I_{\mathrm{SERS}} N_0}{I_0 N_{\mathrm{SERS}}}$$

$I_{SERS}$ and $I_0$ are the peaks intensity of the SERS measurement and the regular Raman measurement, respectively. $N_{SERS}$ and $N_0$ represent the numbers of the corresponding surface and solid molecules effectively excited by the laser beam, respectively. We used the $10^{-10}$ M concentration for an estimate of the ensemble EF. The number of R6G contributing to the Raman signal $N_{Raman}$ was about $4.25 \times 10^{11}$. On the basis of the intensity of the *N*-phenyl stretching mode at 1370 $cm^{-1}$ (Fig. S4, see ESI†), the average EF was calculated to be $2.2 \times 10^9$. The enhancement factor obtained here was compared favourably

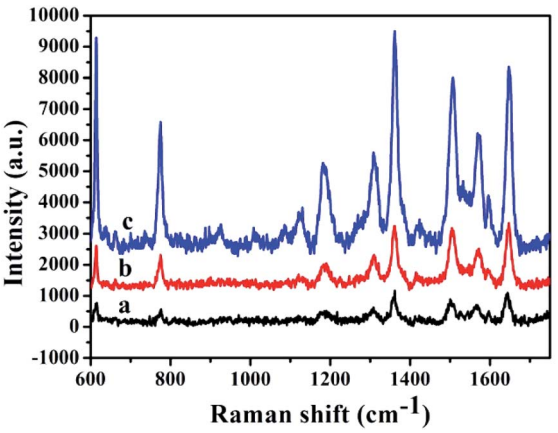


Fig. 4 The SERS spectra of $10^{-7}$ R6G obtained from the assembled MPNCs (curve a), irregular $Fe_3O_4$@Au–Ag nanoparticles (curve b) and assembled $Fe_3O_4$@Au@Ag NAMPCs (curve c). Curve (b) and (c) were vertically shifted.

 

with some of the high ensemble EF values in previous reports (Table S1†). The comparison shown in Table S1† should only serve as an indicator of the SERS substrate performance. By comparing with other SERS substrates, the $Fe_3O_4$@Au@Ag NAMPCs have a medium level of enhancement factor. Combining with other features (*e.g.* uniform signal intensity distribution and high reproducibility), however, the $Fe_3O_4$@Au@Ag NAMPCs are the better SERS substrate.

To investigate the reproducibility and stability of the SERS signal, the assembled $Fe_3O_4$@Au@Ag NAMPCs were immersed in $10^{-6}$ M of CV solution for 1 h. Then, the $Fe_3O_4$@Au@Ag NAMPCs were rinsed repeatedly with deionized water to remove the CV residuals. The intensity of the main vibration of CV from 30 spots of SERS on the $Fe_3O_4$@Au@Ag NAMPCs are shown in Fig. 5. Fig. 5A shows the 2D color coded intensity of the spatiotemporal SERS mapping of CV on the $Fe_3O_4$@Au@Ag NAMPCs. The main Raman vibrations of CV were obviously enhanced at all spots, indicating excellent SERS activity and reproducibility. To get a statistically meaningful result, the relative standard deviation (RSD)[45] of the Raman intensity of the carbon skeleton stretching modes was calculated. Fig. 5 shows the RSD of the Raman vibrations at 914 $cm^{-1}$, 1171 $cm^{-1}$ and 1370 $cm^{-1}$ were 0.0877, 0.0596 and 0.0814, respectively. It clearly reveals the high stability of the SERS signal. The strong SERS signals of the $Fe_3O_4$@Au@Ag NAMPCs suggest that the presence of a high density of the so-called "hot spots" over the assembly results in the high stability of the SERS signal. In order to test the reproducibility between the different batches of $Fe_3O_4$@Au@Ag NAMPCs, we added the same content of CV ($10^{-6}$ M) onto 20 pieces of SERS substrates. Fig. S5 (see ESI†) shows that the RSD of the Raman vibration were all below 15% and proved that the different batches of $Fe_3O_4$@Au@Ag NAMPCs as SERS substrates still have good reproducibility.

### 3.3 Catalysis

Determining the catalytic activity and the reaction kinetics are key issues when new catalysts are developed, characterized, and introduced. *In situ* SERS monitoring of the plasmon-driven surface catalyzed reactions have attracted more and more attention because they open up a new pathway for monitoring and controlling catalyzed reactions on metallic catalysts. In this experiment, control of the plasmon-driven chemical reaction for the transformation of 4-NTP to DMAB by $Fe_3O_4$@Au@Ag NAMPCs was monitored *via in situ* SERS (Scheme 1). This reaction can be dramatically influenced by varying the duration of laser exposure and the laser power. The experimental results show a couple of 4-NTP molecules get 'hot' electrons arising from LSPR and the two 4-NTP molecules transform into a DMAB molecule.[46,47]

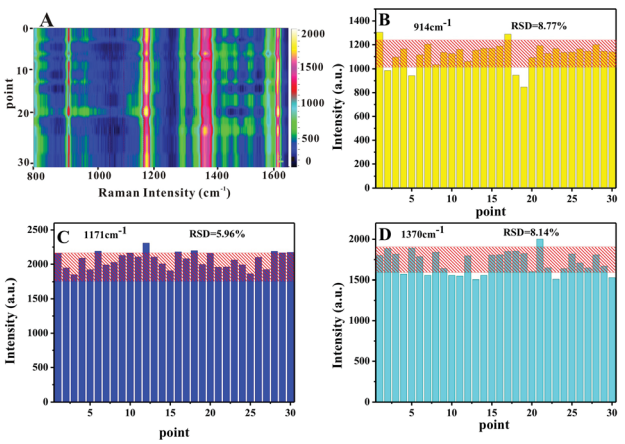


Fig. 5 The 2D color coded intensity of spatiotemporal SERS mapping and the intensities of the main Raman vibrations of CV on the $Fe_3O_4$@Au@Ag NAMPCs.

Fig. 6A shows the principle used to monitor the reaction on the $Fe_3O_4$@Au@Ag NAMPCs using the SERS technique. After adding the 4-NTP, the time-dependent *in situ* SERS spectra of the $Fe_3O_4$@Au@Ag NAMPCs were recorded. The Raman peak at 1099 $cm^{-1}$ in Fig. 6A represents the S–C stretching vibration of 4-NTP. The Raman peaks at 1339 and 1574 $cm^{-1}$ represent the $\nu_s$ ($-NO_2$) ($\nu$-stretching, s-symmetric) and the C–C stretching vibrations of the benzene ring, respectively. The characteristic Raman peak of DMAB is at 1432 $cm^{-1}$, which corresponds to the vibrational modes of N=N. After continuous laser excitation, the $\nu_s$ ($-NO_2$) peak at 1339 $cm^{-1}$ of 4-NTP decreases and the peaks at 1432 $cm^{-1}$ increase, suggesting the gradual conversion of 4-NTP into DMAB, as shown in Fig. 6.[28,48] The reaction can be dramatically influenced by the laser power. In the current experiment, we further investigated the effect of laser power for the reaction rate of catalysis reaction. As shown in Fig. 6A–C, the reaction rate was decreased with reduction of the laser power. Fig. 6D–F is the color coded intensity of spatiotemporal SERS mapping under continuous 632.8 nm laser excitation. In general, the stronger the laser power, the stronger plasmon obtained. Thus, the chemical reaction is more easily triggered by more 'hot' electrons. To quantify the relative reaction rate, we used the peak at 1339 $cm^{-1}$ of 4-NTP and at 1432 $cm^{-1}$ of DMBA as the relative band. As no other agent was used, under continuous illumination and laser excitation, this reaction follows pseudo-second-order kinetics according to the chemical equation. The reaction rate $r$ can be determined by the following equation:[27]

$$r_{4-NTP} = -\frac{1}{2} \times \frac{dc_{4-NTP}}{dt} = kc_{4-NTP}{}^2$$

The reaction rate constant $k$ can be determined using the following equation:[27]

$$kt = \frac{1}{c_{4-NTP}{}^t} - \frac{1}{c^0_{4-NTP}} = \frac{1}{c^0_{4-NTP}} \times \frac{2c_{DMAB}{}^t}{c_{4-NTP}{}^t}$$

$$\frac{c_{DMAB}{}^t}{c_{4-NTP}{}^t} \propto \frac{I_{DMAB}{}^t}{I_{4-NTP}{}^t}$$

$$kt = 2 \times 10^4 \times \frac{I_{DMAB}{}^t}{I_{4-NTP}{}^t} = 2 \times 10^4 \times \frac{I_{1432}}{I_{1339}}$$

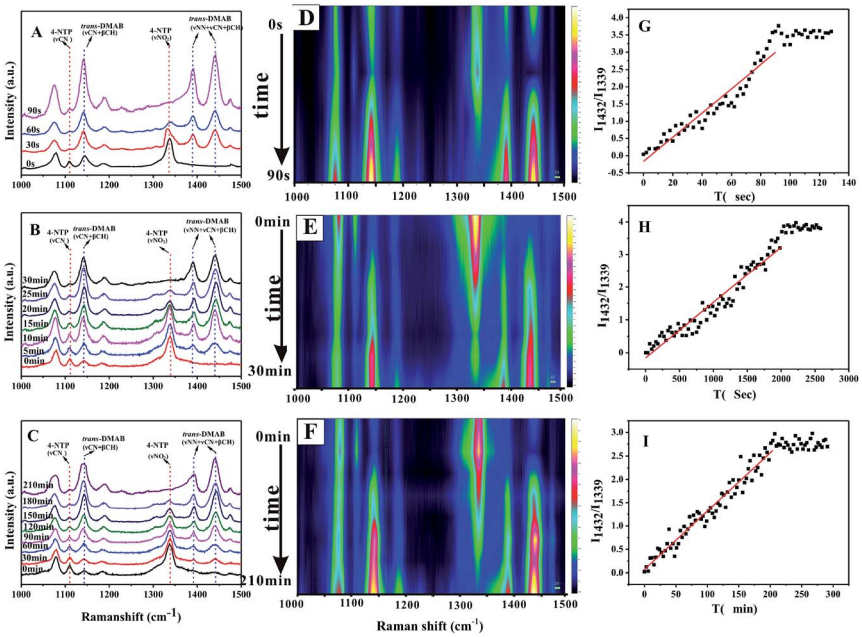


Fig. 6 The SERS spectra of the $Fe_3O_4$@Au@Ag NAMPCs substrate functionalized with 4-NTP at different time intervals after different intensity excitation power: 1 mW (A), 0.5 mW (B) and 0.2 mW (C). The color coded intensity 2D SERS mapping of 4-NTP dimerization into DMAB at an excitation power of 1 mW (D), 0.5 mW (E) and 0.2 mW (F). Determination of the rate constants for the reaction of 4-NTP into DMAB at an excitation power of 1 mW (G), 0.5 mW (H) and 0.2 mW (I).

where $c_{4\text{-NTP}}$ and $c_{\text{DMAB}}$ is the concentration of 4-NTP and DMAB, respectively. $I_{1339}$ and $I_{1432}$ are the intensities of the bands at 1339 cm$^{-1}$ and 1432 cm$^{-1}$, respectively.

Fig. 6G–I show the corresponding plot of $I_{1432}/I_{1339}$ *versus* reaction time $t$, using an excitation power of 1 mW, 0.5 mW and 0.2 mW. Because the relative concentrations of 4-NTP are the same in all the experiments, the apparent rate constants of the reactions catalyzed at 0.2 mW and 0.5 mW are smaller than at 1 mW excitation power giving $k_1 = 2.09 \times 10^{-3}$ s$^{-1}$, $k_{0.5} = 2.02 \times 10^{-4}$ s$^{-1}$ and $k_{0.2} = 4.62 \times 10^{-5}$ s$^{-1}$, respectively. In this dimerization process, the $Fe_3O_4$@Au@Ag NAMPCs adsorbed the 4-NTP molecule through the thiol group and then the molecule receive the hot electrons arising from LSPR of the $Fe_3O_4$@Au@Ag NAMPCs. Finally, the 4-NTP molecules transform into DMAB. Furthermore, the $Fe_3O_4$@Au@Ag NAMPCs and laser power are the two important factors for the plasmon-assisted catalytic process. Fig. 7A shows the SERS spectra of the 4-NTP immersed on the $Fe_3O_4$@Au@Ag NAMPCs under dark conditions. We found that the main SERS signals obtained on the $Fe_3O_4$@Au@Ag NAMPCs after 32 h under dark conditions is similar to the beginning SERS signals of 4-NTP. To investigate the function of the $Fe_3O_4$@Au@Ag NAMPCs in the catalysis of 4-NTP, the 4-NTP was dropped on the silicon wafer without any SERS substrate and exposed to the 632.8 nm laser. However, the Raman signal of the bulk 4-NTP is very low to detect without the SERS substrate. Thus, we added the $Fe_3O_4$@Au NPs into the 4-NTP solution on the silicon wafer and immediately measured the SERS spectra of 4-NTP. Note that the $Fe_3O_4$@Au NPs were used as the SERS substrate, not as plasmonic catalysts in the current experiment. Fig. 7B shows the SERS spectra of the 4-NTP, which is exposed to the 632.8 nm laser without the $Fe_3O_4$@Au@Ag NAMPCs. The main Raman bands of the 4-NTP after 50 min laser irradiation is similar to the beginning SERS signals of 4-NTP. These results demonstrated that the $Fe_3O_4$@Au@Ag NAMPCs and laser are the two essential conditions for the catalysis of 4-NTP.

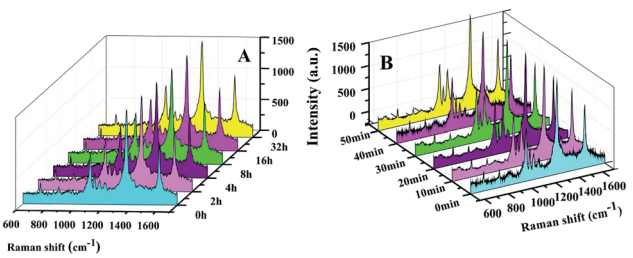


Fig. 7 (A) The Raman spectra obtained at intervals of different times for 4-NTP covered $Fe_3O_4$@Au@Ag NAMPCs under dark conditions. (B) The time-dependent Raman spectra of 4-NTP in the absence of $Fe_3O_4$@Au@Ag NAMPCs under a laser power of 0.5 mW with continuous 632.8 nm laser excitation.

## 4. Conclusions

In summary, we have described the development of 3D assembled $Fe_3O_4$@Au@Ag NAMPCs as a SERS-active substrate, which was constructed from 3D nanoflower shaped silver nanoplates coated on MPNCs *via* a magnetic field induced assembly. The heterogeneous epitaxial growth mechanism was proposed to explain the growth process of the $Fe_3O_4$@Au@Ag NAMPCs. When compared with $Fe_3O_4$@Au MPNCs, the $Fe_3O_4$@Au@Ag

 

NAMPCs significantly enhanced the Raman signal with a SERS enhancement factor of $2.2 \times 10^9$. The relative standard deviation (RSD) of the Raman vibration from 30 spots on the $Fe_3O_4$@Au@Ag NAMPCs and 20 pieces of SERS substrates were all below 15% and revealed the high stability and reproducibility of the SERS signal on the $Fe_3O_4$@Au@Ag NAMPCs. The $Fe_3O_4$@Au@Ag NAMPCs have a highly sensitive and reproducible SERS signals because of their Au/Ag interface, vast surface area and 3D hotspot matrix. Moreover, the $Fe_3O_4$@Au@Ag NAMPCs have double roles as an optical enhancer for SERS detection and as a catalytic substrate for the catalytic reduction of 4-NTP to DMAB. In this experiment, we found that the reaction can be dramatically influenced by varying the duration of laser exposure and the laser power. In this sense, the combined catalytic reactor with built-in non-destructive detection will find broad applications over many reactions in future chemical research.

## Acknowledgements

The authors gratefully acknowledge the financial support from the National Natural Science Foundation of China (Grant no. 21177132, 51272255 and 51502296), Anhui Provincial Natural Science Foundation of China (1608085QE89) and CAS/SAFEA International Partnership Program for creative Research Team of Chinese Academy of Science, P. R. China.

## Notes and references

1 X. M. Zhao, B. H. Zhang, K. L. Ai, G. Zhang, L. Y. Cao, X. J. Liu, H. M. Sun, H. S. Wang and L. H. Lu, *J. Mater. Chem.*, 2009, **19**, 5547–5553.
2 Z. G. Dai, X. H. Xiao, Y. P. Zhang, F. Ren, W. Wu, S. F. Zhang, J. Zhou, F. Mei and C. Z. Jiang, *Nanotechnology*, 2012, **23**, 335701–335707.
3 V. Joseph, C. Engelbrekt, J. D. Zhang, U. Gernert, J. Ulstrup and J. Kneipp, *Angew. Chem., Int. Ed.*, 2012, **51**, 7592–7596.
4 W. Y. Cai, X. H. Tang, B. Sun and L. B. Yang, *Nanoscale*, 2014, **6**, 7954–7958.
5 S. H. Qin, J. Meng, X. H. Tang and L. B. Yang, *Talanta*, 2016, **146**, 452–456.
6 P. Li, B. B. Ma, L. B. Yang and J. H. Liu, *Chem. Commun.*, 2015, **51**, 11394–11397.
7 H. Kim, K. M. Kosuda, R. P. Van Duyne and P. C. Stair, *Chem. Soc. Rev.*, 2010, **39**, 4820–4844.
8 K. N. Heck, B. G. Janesko, G. E. Scuseria, N. J. Halas and M. S. Wong, *J. Am. Chem. Soc.*, 2008, **130**, 16592–16600.
9 P. Liu, H. J. Chen, H. Wang, J. H. Yan, Z. Y. Lin and G. W. Yang, *J. Phys. Chem. C*, 2015, **119**, 1234–1246.
10 K. Zhang, J. J. Zhao, H. Y. Xu, Y. X. Li, J. Ji and B. H. Liu, *ACS Appl. Mater. Interfaces*, 2015, **7**, 16767–16774.
11 K. M. Baek, J. M. Kim, J. W. Jeong, S. Y. Lee and Y. S. Jung, *Chem. Mater.*, 2015, **27**, 5007–5013.
12 K. J. Si, P. Z. Guo, Q. Q. Shi and W. L. Cheng, *Anal. Chem.*, 2015, **87**, 5263–5269.
13 N. T. Panagiotopoulos, N. Kalfagiannis, K. C. Vasilopoulos, N. Pliatsikas, S. Kassavetis, G. Vourlias, M. A. Karakassides and P. Patsalas, *Nanotechnology*, 2015, **26**, 205603.
14 X. Zhou, F. Zhou, H. L. Liu, L. B. Yang and J. H. Liu, *Analyst*, 2013, **138**, 5832–5838.
15 C. Fernandez-Lopez, L. Polavarapu, D. M. Solis, J. M. Taboada, F. Obelleiro, R. Contreras-Caceres, I. Pastoriza-Santos and J. Perez-Juste, *ACS Appl. Mater. Interfaces*, 2015, **7**, 12530–12538.
16 B. N. Khlebtsov, V. A. Khanadeev, E. V. Panfilova, D. N. Bratashov and N. G. Khlebtsov, *ACS Appl. Mater. Interfaces*, 2015, **7**, 6518–6529.
17 H. B. Ni, M. Wang, T. Y. Shen and J. Zhou, *ACS Nano*, 2015, **9**, 1913–1925.
18 Q. Shao, R. H. Que, M. W. Shao, L. Cheng and S. T. Lee, *Adv. Funct. Mater.*, 2012, **22**, 2067–2070.
19 R. H. Que, M. W. Shao, S. J. Zhuo, C. Y. Wen, S. D. Wang and S. T. Lee, *Adv. Funct. Mater.*, 2011, **21**, 3337–3343.
20 H. H. Zhang, M. Liu, F. Zhou, D. L. Liu, G. Q. Liu, G. T. Duan, W. P. Cai and Y. Li, *Small*, 2015, **11**, 844–853.
21 G. Q. Liu, Y. Li, G. T. Duan, J. J. Wang, C. H. Liang and W. P. Cai, *ACS Appl. Mater. Interfaces*, 2012, **4**, 1–5.
22 H. Zhou, J. P. Kim, J. H. Bahng, N. A. Kotov and J. Lee, *Adv. Funct. Mater.*, 2014, **24**, 1439–1448.
23 H. Zhou, S. I. Choi, F. Zou, S. Oh, J. E. Kim, D. Y. Hwang and J. Lee, *ACS Appl. Mater. Interfaces*, 2014, **6**, 19680–19689.
24 H. Zhou, F. Zou, K. Koh and J. Lee, *J. Biomed. Nanotechnol.*, 2014, **10**, 2921–2949.
25 H. S. Shin and S. Huh, *ACS Appl. Mater. Interfaces*, 2012, **4**, 6324–6331.
26 B. H. Liu, G. M. Han, Z. P. Zhang, R. Y. Liu, C. L. Jiang, S. H. Wang and M. Y. Han, *Anal. Chem.*, 2012, **84**, 255–261.
27 X. H. Tang, W. Y. Cai, L. B. Yang and J. H. Liu, *Nanoscale*, 2014, **6**, 8612–8616.
28 L. L. Kang, P. Xu, B. Zhang, H. H. Tsai, X. J. Han and H. L. Wang, *Chem. Commun.*, 2013, **49**, 3389–3391.
29 L. L. Kang, P. Xu, D. T. Chen, B. Zhang, Y. C. Du, X. J. Han, Q. Li and H. L. Wang, *J. Phys. Chem. C*, 2013, **117**, 10007–10012.
30 P. Xu, L. L. Kang, N. H. Mack, K. S. Schanze, X. J. Han and H. L. Wang, *Sci. Rep.*, 2013, **3**, 2997.
31 Z. L. Zhang, M. T. Sun, P. P. Ruan, H. R. Zheng and H. X. Xu, *Nanoscale*, 2013, **5**, 4151–4155.
32 Z. L. Zhang, L. Chen, M. T. Sun, P. P. Ruan, H. R. Zheng and H. X. Xu, *Nanoscale*, 2013, **5**, 3249–3252.
33 Y. F. Huang, H. P. Zhu, G. K. Liu, D. Y. Wu, B. Ren and Z. Q. Tian, *J. Am. Chem. Soc.*, 2010, **132**, 9244–9246.
34 D. Y. Wu, X. M. Liu, Y. F. Huang, B. Ren, X. Xu and Z. Q. Tian, *J. Phys. Chem. C*, 2009, **113**, 18212–18222.
35 V. T. Tran, H. J. Zhou, S. Lee, S. C. Hong, J. Kim, S. Y. Jeong and J. Lee, *ACS Appl. Mater. Interfaces*, 2015, **7**, 8650–8658.
36 Z. L. Yang, S. Chen, P. P. Fang, B. Ren, H. H. Girault and Z. Q. Tian, *Phys. Chem. Chem. Phys.*, 2013, **15**, 5374–5378.
37 H. J. Yin, Z. Y. Chen, Y. M. Zhao, M. Y. Lv, C. A. Shi, Z. L. Wu, X. Zhang, L. Liu, M. L. Wang and H. J. Xu, *Sci. Rep.*, 2015, **5**, 14502.
38 V. Germain, J. Li, D. Ingert, Z. L. Wang and M. P. Pileni, *J. Phys. Chem. B*, 2003, **107**, 8717–8720.
39 L. B. Yang, P. Li, H. L. Liu, X. H. Tang and J. H. Liu, *Chem. Soc. Rev.*, 2015, **44**, 2837–2848.

40 X. H. Xia, J. Zeng, B. McDearmon, Y. Q. Zheng, Q. G. Li and Y. N. Xia, *Angew. Chem., Int. Ed.*, 2011, **50**, 12542–12546.
41 W. Ma, M. Z. Sun, L. G. Xu, L. B. Wang, H. Kuang and C. L. Xu, *Chem. Commun.*, 2013, **49**, 4989–4991.
42 S. T. Sivapalan, B. M. DeVetter, T. K. Yang, T. van Dijk, M. V. Schulmerich, P. S. Carney, R. Bhargava and C. J. Murphy, *ACS Nano*, 2013, **7**, 2099–2105.
43 K. G. Zhang, S. Yao, G. K. Li and Y. L. Hu, *Nanoscale*, 2015, **7**, 2659–2666.
44 A. Hakonen, M. Svedendahl, R. Ogier, Z. J. Yang, K. Lodewijks, R. Verre, T. Shegai, P. O. Andersson and M. Kall, *Nanoscale*, 2015, **7**, 9405–9410.
45 Q. Q. Ding, Y. M. Ma, Y. J. Ye, L. B. Yang and J. H. Liu, *J. Raman Spectrosc.*, 2013, **44**, 987–993.
46 Z. L. Zhang, L. Chen, M. T. Sun, P. P. Ruan, H. R. Zheng and H. X. Xu, *Nanoscale*, 2013, **5**, 3249–3252.
47 W. Xie, B. Walkenfort and S. Schlucker, *J. Am. Chem. Soc.*, 2013, **135**, 1657–1660.
48 Q. Q. Ding, M. D. Chen, Y. Z. Li and M. T. Sun, *Sci. Rep.*, 2015, **5**, 10269.